Mixed magnetism in magnetocaloric materials with first-order and second-order magnetoelastic transitions

Boeije, Maurits; Maschek, Michael; Miao, Xue-Fei; Nguyen, Thang; van Dijk, Niels; Brück, Ekkes

Mixed magnetism in magnetocaloric materials with first-order and second-order magnetoelastic transitions

You may also be interested in:

Mixed magnetism in magnetocaloric materials with first-order and second-order magnetoelastic transitions

M F J Boeije[1], M Maschek, X F Miao, N V Thang, N H van Dijk and E Brück

Fundamental Aspects of Materials and Energy, Faculty of Applied Sciences, Delft University
of Technology, Mekelweg 15, 2629 JB Delft, The Netherlands

E-mail: m.f.j.boeije@tudelft.nl

CrossMark

Abstract

Temperature dependent high-resolution x-ray diffraction measurements were used to characterize the magneto-elastic ferromagnetic transition of $(Fe,Mn)_2(P,Si,B)$ compounds. Across the transition, apart from a change in lattice parameters across the transition, the internal coordinates of Mn and Fe also change. This intrinsic degree of freedom allows Fe in the tetrahedral coordination to decrease the two interatomic distances with the $2c$ position and increase the two distances with the two $1b$ position, while the Fe–Mn distance remains constant. For Mn in the square based pyramidal coordination, all interatomic distances effectively remain constant. Electron density plots show that for second-order transitions, the observed changes are smaller and continuously extending over a wide temperature range in the ferromagnetic and paramagnetic states, due to short-range order. This study shows that the mechanism behind the phase transition in Fe_2P-based materials is an isostructural transition that is equal for both first- and second-order transitions.

Keywords: giant magnetocaloric effect, first-order phase transitions, electron density plots, magnetoelastic coupling, x-ray diffraction

(Some figures may appear in colour only in the online journal)

1. Introduction

The magnetocaloric effect is characterized by an adiabatic temperature change under the application of a magnetic field. It is a promising technique to replace the conventional vapour compression technology because of the increased efficiency, which can be 20–30% higher [1]. Furthermore, the refrigerants are solids, which are more environmentally friendly compared to the greenhouse gases that are used in traditional cooling techniques. Additionally, by cooling or heating the material, the magnetization changes significantly, which can be used to generate electricity from waste heat [2].

In the last two decades, research into magnetocaloric materials has intensified due to the discovery of so-called giant magnetocaloric materials [3]. These materials have a magnetocaloric effect that is enhanced by the presence of latent heat. For Fe_2P-based materials, the nature of the ferromagnetic transition is reflected by a discontinuous change in unit-cell parameters [4, 5]. When the lattice parameters change discontinuously, the magnetic transition is of first order (FOMT) and is generally accompanied by latent heat and hysteresis. When there is no jump in lattice parameters, the magnetic transition is of second order (SOMT), without latent heat or hysteresis.

The transition can be modeled considering the change in Gibbs free energy across the magnetic phase transition, as described in the Landau model [6, 7]:

$$\Delta G = \frac{\alpha}{2}M^2 + \frac{\beta}{4}M^4 + \frac{\gamma}{6}M^6 - \mu_0 HM \qquad (1)$$

J. Phys. D: Appl. Phys. **50** (2017) 174002

M F J Boeije *et al*

Figure 1. Unit cell of the hexagonal Fe_2P structure (space group $P\bar{6}2$ m) showing the Wyckoff positions and the layered structure. The 1 *b* and 2 *c* positi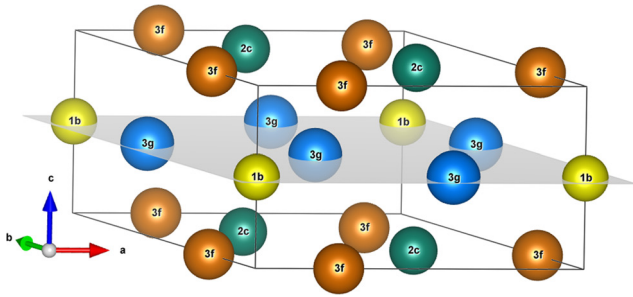ons are occupied by the nonmetal P and Si atoms and the 3 *f* and 3 *g* positions are occupied by metal Fe and Mn atoms.

where the magnetization M is the order parameter and $\mu_0 H$ the applied magnetic field. Parameter $\alpha = \alpha_0(T - T_0)$ depends on temperature with respect to a characteristic temperature T_0 and α_0, β, γ are constants ($\alpha_0, \gamma > 0$). Minimization with respect to the magnetization M ($\partial \Delta G / \partial M = 0$) leads to the equation of state:

$$\alpha + \beta M^2 + \gamma M^4 = \frac{\mu_0 H}{M} \tag{2}$$

where β can be positive or negative, leading to a second-order or first-order magnetic transition, respectively. For $\beta = 0$ (critical point), the transition is on the verge of a first-order magnetic transition. Material properties in the vicinity of such a critical point (CPT) are of great interest for applications. For near room temperature cooling, materials with a small negative value for β show a sizeable latent heat in combination with a low hysteresis. For heat conversion, materials with a small positive value for β show a steep magnetization increase without latent heat.

To study the difference between strongly first-order, second-order and near-critical behaviour, we studied three samples with high-resolution powder x-ray diffraction (PXRD) as a function of temperature. The critical temperature and the character of the phase transition can easily be tuned by balancing the Mn/Fe and P/Si ratios [8]. The addition of B, N and C causes a tempering of the first-order transition and leads to a simultaneous increase in T_C [9–11].

As shown in figure 1, Fe_2P has a hexagonal unit cell (space group $P\bar{6}2$ m) containing two layers of atoms. Both layers contain magnetic and nonmagnetic atoms. For $(Mn,Fe)_2(P,Si)$ there is a site preference for Mn on the 3 *g* position, Fe prefers the 3 *f* position and Si prefers the 2 *c* position [12]. While the nonmagnetic atoms occupy fixed relative positions, the magnetic atoms have a translational degree of freedom, which has not been systematically investigated so far.

Recently, the origin of the giant magnetocaloric effect in Fe_2P-based materials was experimentally established [13]. The basis for this effect lies in a special kind of two sublattice magnetism where both weak and strong magnetism is present and is distinctly different from conventional two-sublattice magnetism [14]. One of these sublattices is governed by strong magnetism (3*g* site) and the size of the moments is relatively stable across the transition. The other sublattice

is governed by weak magnetism (3*f* site) and the moment is strongly reduced in magnitude. This phenomenon was named *mixed magnetism* [15]. The strong reduction of the moment of one sublattice in the paramagnetic state was linked to the strengthening of a covalent bond between magnetic and metalloid atoms, which was made clear by investigating electron density difference plots. The change in magnetic moment and interatomic distance bears resemblance to high-spin to low-spin transitions [16] and Jahn–Teller distortions [17], found in localized systems. This study uses the electron density plots to characterize the difference in behaviour between first- and second-order magnetic transitions.

2. Experimental

Powders of Mn, Fe, P, Si and B were mixed together in a ball milling device and milled for 10 h. The obtained powder was pressed into cylinders that were sealed in quartz ampoules filled with 10 kPa Ar, sintered at 1100 °C for 2 h, annealed at 850 °C for 20 h and quenched to room temperature. High-resolution powder x-ray diffraction (PXRD) was performed at the ESRF at beamline BM01A using a wavelength of 0.688 84 Å. The temperature control was achieved using a N_2 Cryostream. The temperature range between 100 and 400 K was covered in temperature steps of 5 K. The samples were put in 0.5 mm capillaries and spun. Rietveld refinement was performed using the FullProf software [18]. The electron density was calculated by VESTA [19] and processed in Matlab.

3. Results

Three samples were measured as a function of temperature. The first sample with composition $MnFeP_{0.6}Si_{0.4}$ shows a FOMT, the second sample with composition $Mn_{1.7}Fe_{0.3}P_{0.4}Si_{0.6}$ shows a SOMT and the third sample with composition $MnFeP_{0.595}Si_{0.33}B_{0.075}$ shows a CPT. The temperature evolution of the $\{3\,0\,0\}$, $\{2\,1\,1\}$ and $\{0\,0\,2\}$ PXRD reflections upon heating is shown in figure 2. The effect of temperature on the unit cell is directly visible. For the sample with a FOMT, the a and c-axes change discontinuously and there is a region of phase coexistence. For the sample with a SOMT, the unit cell changes continuously and no region of phase coexistence is detected. For the CPT sample, a rapid continuous change of the lattice parameters is present at T_C. The value of T_C is 275, 205 and 295 K for the FOMT, SOMT and CPT, respectively.

While inspection of the raw data gives qualitative information, quantitative information can be extracted using Rietveld refinement. The refinement is shown in figure 3 and the parameters are listed in table 1. To directly compare the materials, which have different unit-cell volumes and transition temperatures, the normalized data are plotted in figure 4. Far below T_C, both the a and c axis show a similar temperature dependence. When the temperature is close to T_C, there is an abrupt change for the FOMT and a more gradual change for the SOMT sample. At the same time, the FOMT shows a much larger overall change in lattice parameters compared to the SOMT.
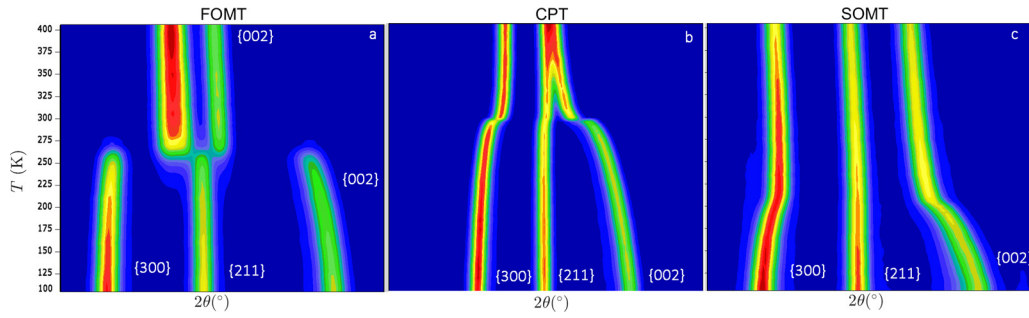
Figure 2. Intensity of scattering angle (2θ) as a function of temperature (T) for $MnFeP_{0.6}Si_{0.4}$ (a), $MnFeP_{0.595}Si_{0.33}B_{0.075}$ (b) and $Mn_{1.7}Fe_{0.3}P_{0.4}Si_{0.6}$ (c). The $\{300\}$, $\{211\}$ and $\{002\}$ peaks are shown as the material crosses the transition upon heating.

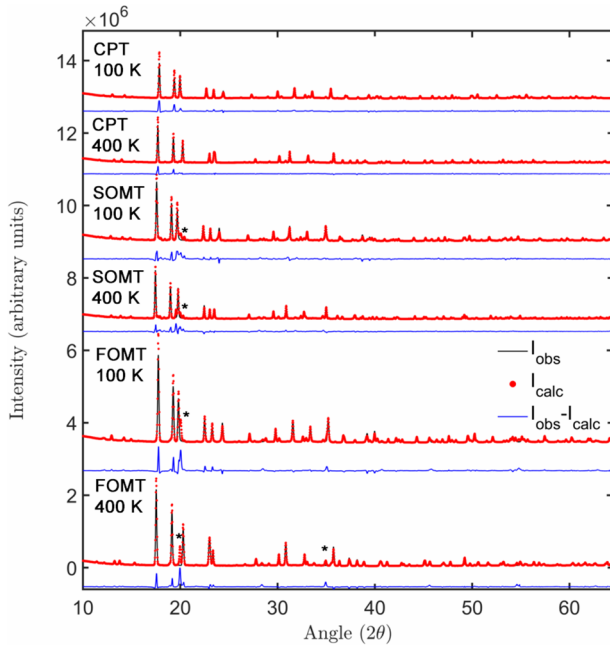**Figure 3.** X-ray powder diffraction patterns and refinements of $MnFeP_{0.6}Si_{0.4}$ (FOMT), $MnFeP_{0.595}Si_{0.33}B_{0.075}$ (CPT) and $Mn_{1.7}Fe_{0.3}P_{0.4}Si_{0.6}$ (SOMT) measured at 100 K and 400 K. The asterisk denotes the $(Fe,Mn)_3Si$ second phase, which was not included in the refinement.
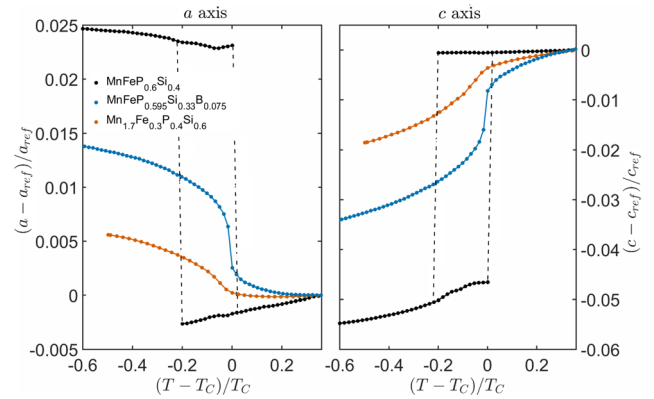

Figure 4. Reduced lattice parameters as a function of reduced temperature, where $x_{ref} = x(T_C + 100\,\text{K})$. T_C values are 275, 205 and 295 K for the FOMT, SOMT and CPT respectively.

Table 1. Refined x-ray diffraction data at 400 K. The $3g$ positions are located at $(x, 0, \frac{1}{2})$ and the $3f$ positions at $(x, 0, 0)$.

	FOMT	CPT	SOMT
S.G.	P $\bar{6}$ 2 m	P $\bar{6}$ 2 m	P $\bar{6}$ 2 m
a (Å)	5.969(9)	5.984(7)	6.126(0)
c (Å)	3.458(7)	3.375(3)	3.384(1)
x_g	0.589(3)	0.592(9)	0.592(6)
x_f	0.248(8)	0.251(7)	0.252(8)
B_{3g} (Å^2)	1.089(5)	0.824(3)	1.119(0)
B_{3f} (Å^2)	0.930(9)	0.860(9)	1.055(1)
B_{2c} (Å^2)	1.066(6)	0.398(9)	0.807(0)
B_{1b} (Å^2)	1.083(3)	0.938(2)	1.444(3)
R_p	5.56	3.93	6.87
R_{wp}	5.76	4.04	5.26

The total change across the transition for all three samples is summarized in table 2. Although the lattice parameters change significantly, the change in cell volume is limited. This absence of a volume change is beneficial for applications, as it reduces hysteresis and cracking during cycling. Surprisingly, the internal parameters x_f and x_g show the same sign as the change in the a axis.

The temperature dependence of the internal coordinates x_f and x_g are shown in figure 5. The uncertainty in the phase coexistence region of the FOMT sample is significantly larger due to the phase fraction. For that reason, the coordinate values have been omitted in this region.

From the atomic coordinates and lattice parameters, the interatomic distances can be calculated in the FM and PM states for all samples. The distances are given in table 3.

The diffraction patterns can also be used to investigate the electron density, using the structure factors obtained in the refinement. By taking the difference between the FM and PM states, an electron density difference plot can be constructed. This is only valid after normalization of the data. While the total electron density in the unit cell does not change with temperature, the diffracted intensity decreases with increasing temperature due to thermal diffuse scattering. The sum of all the structure factors should remain constant when multiplied by a temperature-dependent correction factor. This procedure was used to obtain the normalization constant.

Table 2. Relative change in cell parameters (%) across the transition with respect to the low temperature (ferromagnetic) phase ($\frac{\Delta n}{n_{FM}}$). For the SOMT sample, the properties at $T_C - 20$ K were used.

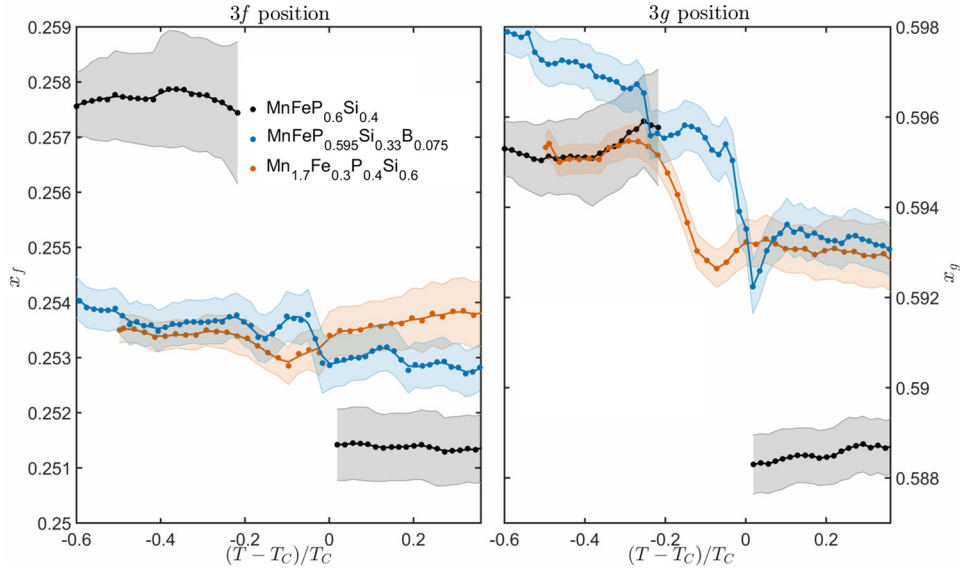| Composition		a	c	c/a	V	x_f	x_g
$MnFeP_{0.6}Si_{0.4}$	FOMT	-2.64	4.98	10.7	-0.06	-2.41	-1.21
$MnFeP_{0.595}Si_{0.33}B_{0.075}$	CPT	-0.64	0.93	2.01	-0.05	-0.36	-0.62
$Mn_{1.7}Fe_{0.3}P_{0.4}Si_{0.6}$	SOMT	-0.21	0.43	0.73	-0.13	-0.20	-0.60

Figure 5. Internal coordinates x_f and x_g as a function of the reduced temperature. The data points in the phase coexistence region of the FOMT sample were not included because of the large uncertainty. The error bars are represented as a shaded region around the curve.

Table 3. Interatomic distances in the FM and PM state (Å).

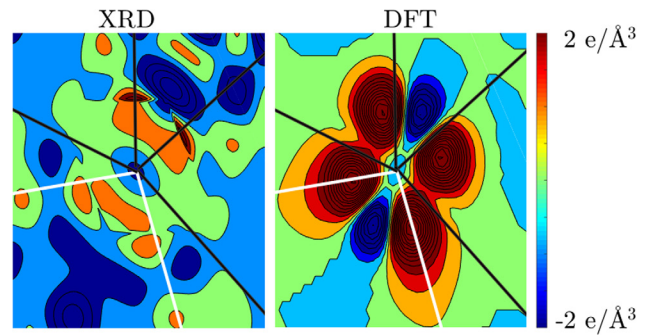|	FOMT		CPT		SOMT	
	FM	PM	FM	PM	FM	PM
$3f-1b$	2.271	2.287	2.253	2.259	2.281	2.288
$3f-2c$	2.305	2.270	2.289	2.280	2.330	2.323
$3g-1b$	2.480	2.494	2.445	2.444	2.492	2.490
$3g-2c$	2.480	2.453	2.470	2.470	2.501	2.505
$3f-3g$	2.643	2.650	2.644	2.641	2.673	2.674

Figure 6. The electron density difference plots of the PM state minus the FM state for the FOMT sample (left) and a DFT calculation (right) with Fe at the centre. The positive parts are associated with the PM state and the negative parts are associated with the FM state. The white lines are directed towards the Si atoms and the black lines are directed towards other Fe atoms.

For the sample with a FOMT, there is a temperature where the FM phase coexists with the PM phase. In this region, the electron density difference between these two phases can be obtained without applying a temperature-dependent normalization. The Fe atom was used as centre. The electron density difference is plotted in figure 6 as a 2D colour map in the $a - b$ plane around Fe, both for the experimental data and for the data obtained by DFT calculations. Details on the method are described in a previous paper [13].

For the other samples, there is no region of coexistence and the difference between the two phases can only be shown by subtracting the electron density above and below the transition. The results for all three samples in the $a - b$ plane are shown in figure 7. The features around Fe are similar for all

three samples, they show a 'dipole' caused by the atomic shift and a region of high density parallel to the (110) direction. Around Si the data do not show a consistent picture for the FOMT, CPT and SOMT samples. The electron density difference plots comparing the PM state far above the transition and just above the transition are shown in figure 8. For these plots, the features around Fe are still visible for the SOMT sample, but are absent for the other samples.
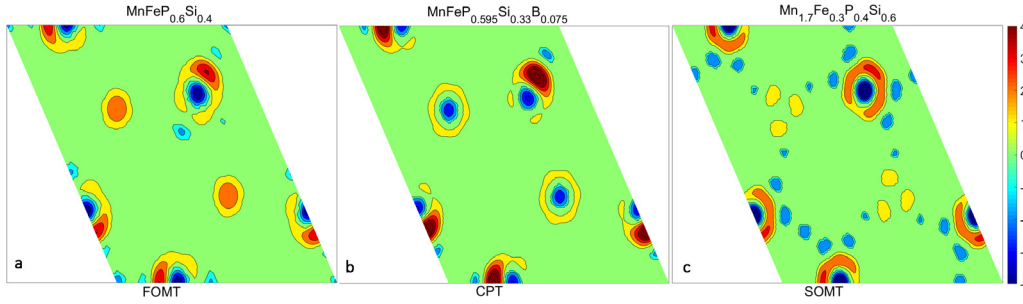
Figure 7. Electron density difference plots, between the PM phase far above the transition ($T = T_C + 100$ K) and the FM phase just below the transition ($T = T_C - 20$ K). The shift in atomic coordinates of the 3*f* position (preferentially occupied by Fe) is recognizable by the dipole. The positive (PM) electron density is oriented towards Si and the negative (FM) electron density along the diagonal. The main features are similar for all three samples. The scale is in $e \ \mathring{A}^{-3}$.
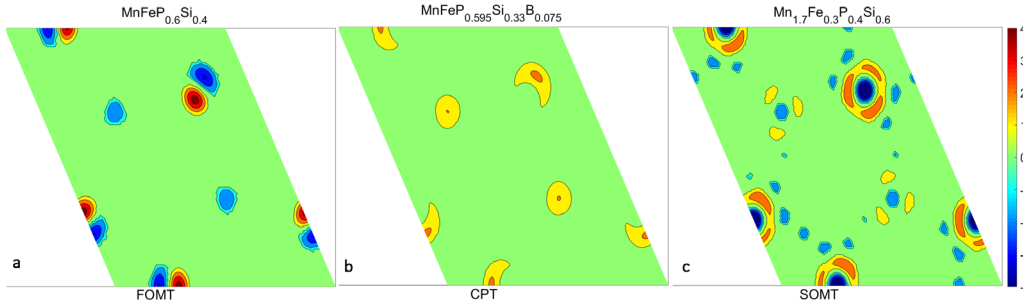

Figure 8. Electron density difference plots, between the PM phase far above the transition ($T = T_C + 100$ K) and the PM phase just above the transition ($T = T_C + 20$ K). The scale is in $e \ \mathring{A}^{-3}$.

4. Discussion

The difference in behaviour between the three samples becomes most apparent when we look at the change in lattice parameters. The change in lattice parameters for the FOMT sample is about $5\times$ more pronounced compared to the CPT sample and about $10\times$ compared to the SOMT sample. For these compositions, the changes in lattice parameters hardly affect the volume; the volume change is 1 to 2 orders of magnitude lower. Apparently, the substitution of P for B, which leads to a smaller unit cell, has a profound effect on the transition. However, the size of the unit cell is not the only factor that decreases the magnitude of the effect, for the SOMT sample has the largest unit cell.

The change in lattice parameters with respect to the linear expansion observed in the PM state corresponds to the elastic strain originating from the ferromagnetic order. When the elastic energy and a bilinear magnetoelastic coupling are included, the change in Gibbs free energy becomes:

$$\Delta G = \frac{\alpha}{2}M^2 + \frac{\beta}{4}M^4 + \frac{\gamma}{6}M^6 - \mu_0 HM + 1/2 \sum_{i,j} C_{ij}e_i e_j + \sum_i \xi_i e_i M \tag{3}$$

where C_{ij} are elastic constants, e_i is the elastic strain and ξ_i is the magnetoelastic coupling constant. Since the hexagonal symmetry of the system is not broken by the ferromagnetic order, only the tensile strains within the basal plane $e_i = \Delta a/a$ and along the sixfold axis $e_3 = \Delta c/c$ will develop:

$$\frac{e_1}{M} = \frac{\xi_1 C_{33} - \xi_3 - C_{13}}{2C_{13}^2 - C_{33}(C_{11} + C_{12})} \tag{4a}$$

$$\frac{e_3}{M} = \frac{\xi_3(C_{11} + C_{12}) - 2\xi_1 C_{13}}{2C_{13}^2 - C_{33}(C_{11} + C_{12})}. \tag{4b}$$

As can be seen in table 2, all three materials have been chosen to have a low volume change across the transition. In this case we find $e_v = 2e_1 + e_3 \approx 0$. We therefore define $e \equiv e_1 \approx -\frac{1}{2}e_3$. The change in *c/a* ratio is characteristic for the transformation strain and amounts to $\Delta(c/a)/(c/a) = e_3 - e_1 \approx -3e$. In this case the magnetoelastic coupling constants can be deduced from the dependence of the transformation strain on the order parameter M:

$$\xi_1 \approx (2C_{13} - C_{11} - C_{12})\frac{\partial e}{\partial M} \tag{5a}$$

$$\xi_3 \approx (C_{13} - C_{33})\frac{\partial e}{\partial M}. \tag{5b}$$

In figure 9 the scaled transformation strains e_1 and $-\frac{1}{2}e_3$ are plotted as a function of the normalized magnetization M. The linear dependence between the transformation strain and the magnetization confirms the presence of a bilinear magnetoelastic coupling around T_C, and indicates that higher order terms are not required to describe the system. From the experimental slopes and the calculated elastic constants [20], the magnetoelastic coupling parameters listed in table 4 are
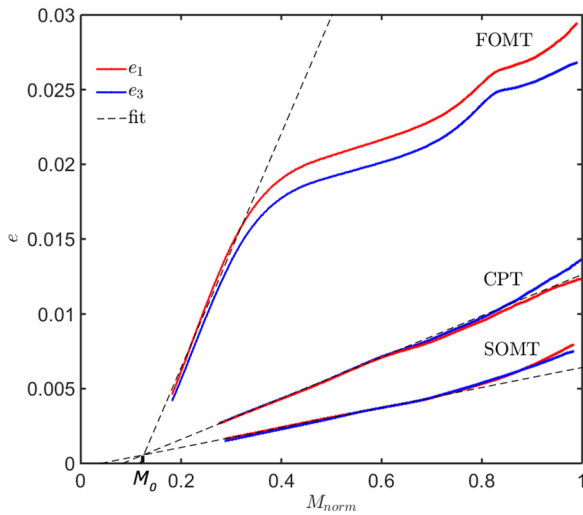
J. Phys. D: Appl. Phys. 50 (2017) 174002

M F J Boeije et al

Figure 9. Strain $e = e_1 \approx -\frac{1}{2}e_3$ as a function of the normalized magnetization at $T = 100$ K. Linear fits around T_C show that the coupling constants ξ are largest for the FOMT sample, followed by the CPT and SOMT samples. M_0 is the induced magnetization above T_C by the magnetic field of 1 T.

Table 4. Experimentally obtained values of $\partial e/\partial M$ (m A^{-1}) and the corresponding values of the magnetoelastic coupling constants (10^3 N Am^{-1}) for MnFeSi$_{0.33}$P$_{0.66}$ in the FM state calculated using the elastic constants [20].

	$\frac{\partial e}{\partial M}$	ξ_1	ξ_2
FOMT	11.7	1.17	−1.95
CPT	1.54	0.15	−0.25
SOMT	0.98	0.10	−0.14

deduced. The elastic constants $C_{11}, C_{12}, C_{13}, C_{33}, C_{44}$ and C_{66} are 308.3, 79.5, 114.0, 227.8, 119.5 and 114.4 GPa, respectively [20].

All linear fits intersect at M_0 due to the tail above T_C, induced by the applied field of 1 T. It also gives a small deviation in the lattice parameters compared to the linear expansion, shifting the data up. A clear trend is visible: the coupling is strong for the FOMT sample and decreases as the transition becomes second order.

Given the change in lattice parameters across the transition, we can investigate the influence of the relative position of the atoms on the $3g$ (Mn) and $3f$ (Fe) site, respectively. Because the ferromagnetism of the low temperature phase restrains the total symmetry of the system because of the broken time-inversion symmetry, going to a paramagnetic state could increase the total symmetry. In this case this could manifest itself due to the appearance of an inversion center in the crystallographic unit cell. The relative positions of Mn and Fe could assume a value ($x = 0.5$) where the total symmetry is increased due to an inversion center. However, the actual values for x are not close to this symmetry point and the symmetry cannot be increased this way. Instead, it is more insightful to focus on the changing interatomic distances.

For Mn, the change in the unit cell is large for the FOMT sample and would result in a 3% change in Mn–$1b$ distances. However, when the shift in the internal coordinate is taken into

account, we see that the distance only changes by about 1%. The change in x_g-parameter therefore partially compensates for the change in unit cell parameters. However, when we look at the SOMT and CPT samples, it is found that the lattice parameter change is compensated by the internal parameter of Mn so that both Mn-X distance changes are effectively zero. This has been illustrated in figure 10.

For the layer preferentially occupied by Fe, this is not the case. For the SOMT sample, there is also a compensation point at $x_f = 0.25$, but Fe only shows a partial shift to this position. This results in a reduced, but finite change in distance. The Fe-occupied layer must play an active role in the transition, as was predicted earlier [15]. The fact that this behaviour is observed for all samples, indicates that the mechanism behind the transition is also similar.

To illustrate the changes, it is useful to consider the atomic environment around the magnetic $3f$ and $3g$ sites, as shown in figure 11. The $3f$ site has a tetrahedral coordination with two $2c$ and $1b$ sites at unequal distances (see table 3). The $3g$ site has a square-based pyramidal coordination with four $2c$ sites and one $1b$ site. From figure 10 it is clear that the distances in the tetrahedral polyhedron change across the transition, while the distances in the square-based pyramidal polyhedron hardly change.

This magnetoelastic transition can therefore be viewed as an isostructural phase transition. The first crystal structure (hex1) has 'large' interatomic distances in the $a - b$ plane, the second (hex2) has 'small' interatomic distances. While the structural properties of both phases can easily be probed, the magnetic properties of both phases cannot be easily probed. For the low temperature phase the magnetization is known, while for high temperatures T_C is known. Recent calculations [13] show that the moments size for hex2 is significantly lower compared to hex1. The value of T_C can be estimated using the spin fluctuation temperature T_{SF}, as proposed by Mohn and Wohlfarth [21, 22]

$$T_C \propto T_{SF} = \frac{M_0^2}{10k_B\chi_0}, \tag{6}$$

where M_0 is the average magnetic moment per atom in μ_B at 0 K and χ_0 is the exchange enhanced susceptibility at equilibrium which includes the exchange parameter I

$$\chi_0^{-1} = \left(\frac{1}{4\mu_b^2}\right)(1/N^+(\epsilon_F) + 1/N^-(\epsilon_F)) - 2I. \tag{7}$$

Using equation (6), the reduction of the moment in one sublattice leads to a decrease of the T_C by a factor of 2–3, based on previous calculations [13, 23]. The fact that the T_C values for all samples are in the same range, leads us to believe that the reduced moment in the paramagnetic phase is present in all samples.

So far, the discussion has focused on the similarities between the samples, which all transform from hex1 to hex2. It is also important to investigate the difference between the FOMT and SOMT samples. For that reason, we focus on the electron density difference plots just above and below the phase transition, as shown in figures 7 and 8. Apart from the
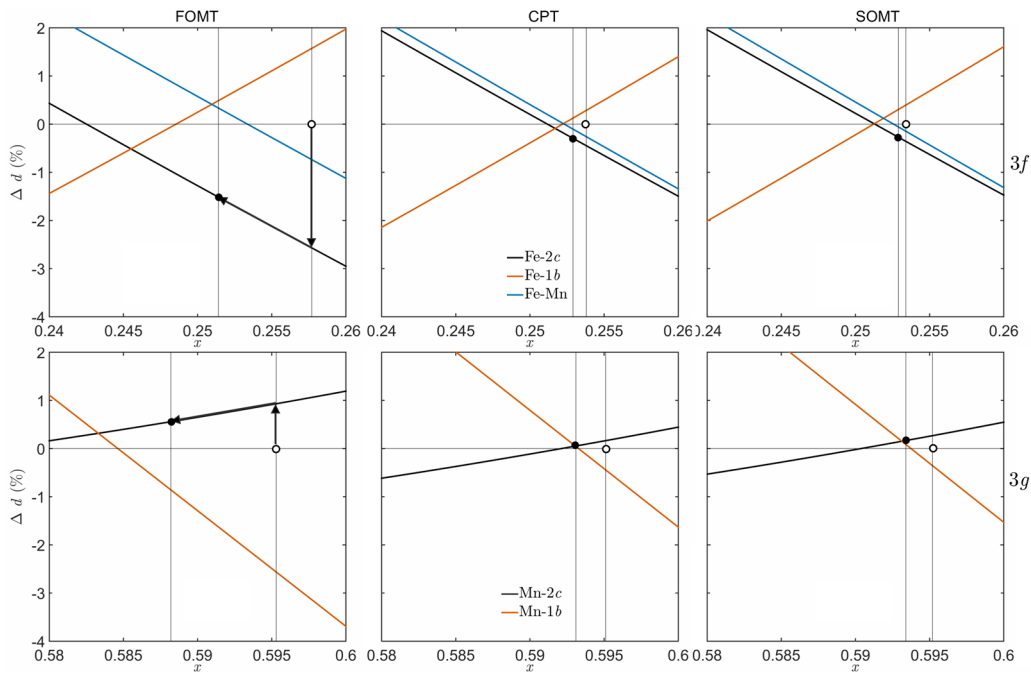
Figure 10. Change in interatomic distances Δd induced by the lattice parameters as a function of internal x-coordinate of Fe and Mn for the FOMT, CPT and SOMT samples. The arrows illustrate the changes for both M–2c distances in the FOMT sample: across the transition, the distance decreases (vertical line) due to the change in lattice parameters. In addition, the relative position of Fe changes (diagonal line), the combined distance change is between the original position (open circle) and final position (closed circle).
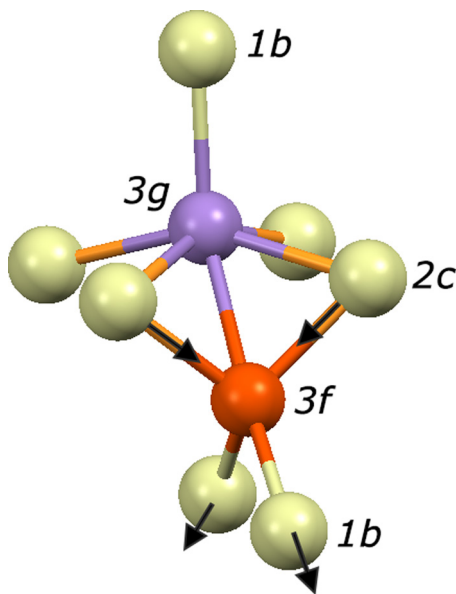

Figure 11. Tetrahedral and square-based pyramidal coordination polyhedra around the 3f and 3g sites, respectively. Across the transition, all samples show a change in the tetrahedron, moving the 2c position closer and elongating the distance to 1b. For the FOMT sample the changes are large enough to affect the 3g distances. No appreciable change in coordination takes place.

dipole feature on the 3f site, there is also a redistribution of electron density around this site. All three samples show this, although with different contrast. When crossing the transition, this feature disappears for the FOMT and CPT samples, but not for the SOMT sample. This suggests that for the SOMT sample, the electronic redistribution is not complete

in this temperature interval. We believe that short-range order that is found to extend far into the paramagnetic state in this material, is an important effect that causes a more gradual continuous change in the electronic structure [24].

5. Conclusion

In summary, the structural and electronic properties of (Fe,Mn)$_2$(P,Si,B) samples with a FOMT, CPT and SOMT have been studied. Both the lattice parameters and the internal coordinates of Mn and Fe change across the transition. For Fe in the tetrahedral coordination the two interatomic distances with the 2c position decrease and the two distances with the two 1b position increase, while the Fe–Mn distance remains constant. For Mn in the square based pyramidal coordination, all interatomic distances remain constant. For the FOMT sample the changes cannot be accommodated and the sample subsequently shows a large thermal hysteresis. The changes in the tetrahedral arrangement around Fe are similar for all samples and the transitions can be viewed as an isostructural transition resulting in different magnetic properties. Both the changes in interatomic distances and the electron density plots clearly show that the mechanism is the same for all samples. In addition, the T_C of the samples is much lower compared to the estimated T_C, based on the low temperature phase. It is not yet clear what factors govern the sharpness of the transition, but based on the electron density difference plots it is clear for the SOMT sample the observed changes are smaller and continuously extending over a wide temperature range in the paramagnetic state, probably due to short-range order.

Acknowledgments

References

[1] Gschneidner K A Jr and Pecharsky V K 2008 Thirty years of near room temperature magnetic cooling: where we are today and future prospects *Int. J. Refrig.* **31** 945–61

[2] Vuarnoz D, Kitanovski A, Gonin C, Borgeaud Y, Delessert M, Meinen M and Egolf P W 2012 Quantitative feasibility study of magnetocaloric energy conversion utilizing industrial waste heat *Appl. Energy* **100** 229–37

[3] Tegus O, Brück E, Buschow K H J and de Boer F R 2002 Transition-metal-based magnetic refrigerants for room-temperature applications *Nature* **415** 150–2

[4] Rundqvist S and Jellinek F 1959 The structures of Ni_6Si_2B and Fe_2P and some related phases *Acta Chem. Scand.* **13** 425–32

[5] Lundgren L, Tarmohammed G, Beckman O, Carlsson B and Rundqvist S 1978 First order magnetic phase transition in Fe_2P *Phys. Scr.* **17** 39–48

[6] Landau L D 1937 On the theory of phase transitions. I. *Zh. Eksp. Teor. Fiz.* **7** 19–32

[7] Magnus A, Carvalho G, Coelho A A, Gama S, Gandra F C G, von Ranke P J and de Oliveira N A 2009 Investigation of the first-order metamagnetic transitions and the colossal magnetocaloric effect using a landau expansion applied to MnAs compound *Eur. Phys. J.* B **68** 67–72

[8] Dung N H, Zhang L, Ou Z Q and Brück E 2011 From first-order magneto-elastic to magneto-structural transition in $(Mn,Fe)_{1.95}P_{0.50}Si_{0.50}$ compounds *Appl. Phys. Lett.* **99** 092511

[9] Thang N V, Miao X F, van Dijk N H and Brück E 2016 Structural and magnetocaloric properties of $(Mn,Fe)_2(P,Si)$ materials with added nitrogen *J. Alloys Compd.* **670** 123–7

[10] Guillou F, Porcari G, Yibole H, van Dijk N H and Brück E 2014 Taming the first-order transition in giant magnetocaloric materials *Adv. Mater.* **27** 2671

[11] Miao X F, Thang N V, Caron L, Yibole H, Smith R I, van Dijk N H and Brück E 2016 Tuning the magnetoelastic transition in $(Mn,Fe)_2(P,Si)$ by B, C, and N doping *Scr. Mater.* **124** 129–32

[12] Miao X F, Caron L, Roy P, Dung N H, Zhang L, Kockelmann W A, de Groot R A, van Dijk N H and Brück E 2014 Tuning the phase transition in transition-metal-based magnetocaloric compounds *Phys. Rev.* B **89** 174429

[13] Boeije M F J, Roy P, Guillou F, Yibole H, Miao X F, Caron L, Banerjee D, van Dijk N H, de Groot R A and Brück E 2016 Efficient room-temperature cooling with magnets *Chem. Mater.* **28** 4901–05

[14] Skomski R 1998 Finite-temperature behavior of anisotropic two-sublattice magnets *J. Appl. Phys.* **83** 6724–6

[15] Dung N H, Ou Z Q, Caron L, Zhang L, Thanh D T C, de Wijs G A, de Groot R A, Buschow K H J and Brück E 2011 Mixed magnetism for refrigeration and energy conversion *Adv. Energy Mater.* **1** 1215–9

[16] Bhide V G, Rajoria D S, Rao G R and Rao C N R 1972 Mössbauer studies of the high-spinlow-spin equilibria and the localized-collective electron transition in $LaCoO_3$ *Phys. Rev.* B **6** 1021–32

[17] Millis A J, Shraiman B I and Mueller R 1996 Dynamic Jahn–Teller effect and colossal magnetoresistance in $La_{1-x}Sr_xMnO_3$ *Phys. Rev. Lett.* **77** 175–8

[18] Rodríguez-Carvajal J 1990 *Satellite Meeting on Powder Diffraction of the XV IUCr Congress* p 127

[19] Momma K and Izumi F 2011 Vesta 3 for three-dimensional visualization of crystal, volumetric and morphology data *J. Appl. Crystallogr.* **44** 1272–6

[20] Roy P, Torun E and de Groot R A 2016 Effect of doping and elastic properties in $(Mn,Fe)_2(Si,P)$ *Phys. Rev.* B **93** 094110

[21] Mohn P and Wohlfarth E P 1987 The Curie temperature of the ferromagnetic transition metals and their compounds *J. Phys. F: Met. Phys.* **17** 2421–30

[22] Mohn P 2003 *Magnetism in the Solid State* (Berlin: Springer)

[23] Roy P, Brück E and de Groot R A 2016 Latent heat of the first-order magnetic transition of $MnFeSi_{0.33}P_{0.66}$ *Phys. Rev.* B **93** 165101

[24] Miao X F *et al* 2016 Short-range magnetic correlations and spin dynamics in the paramagnetic regime of $(Mn,Fe)_2(P,Si)$ *Phys. Rev.* B **94** 014426